SCIENTIFIC REP♂RTS

OPEN

Cooperative light scattering from helical-phase-imprinted atomic rings

H. H. Jen[1], M.-S. Chang[2] & Y.-C. Chen[2]

We theoretically investigate the light scattering of super- and subradiant states of an atomic ring prepared by single excitation with a photon which carries an orbital angular momentum (OAM). For excitations with linear polarizations, the helical phase imprinted (HPI) atomic ring presents a discrete C_4 rotational symmetry when number of atoms $N = 4n$ with integers n, while for circular polarizations with arbitrary N, the continuous and C_N symmetries emerge for the super- and subradiant modes, respectively. The HPI superradiant modes predominantly scatter photons in the forward-backward direction, and the forward scattering can be further enhanced as atomic rings are stacked along the excitation direction. The HPI subradiant modes then preferentially scatter photons in the transversal directions, and when rings are stacked concentrically and on a plane, crossover from sub- to superradiance is observed which leads to splitting and localization of the far-field scattering patterns in the polar angle. The HPI super- and subradiant states are thus detectable through measuring the far-field radiation patterns, which further allow quantum storage and detection of a single photon with an OAM.

Controlled strong light-matter interactions in quantum optical systems for efficient generation, storage, and manipulation of quantum correlations[1] is essential for establishing robust long-distance quantum entanglement for quantum communication[2–4] and quantum network[5]. This has also spurred the development of quantum memory and quantum repeater in recent years[6], which stores and relays entanglement. Quantum correlation in an atomic system is often arisen through spontaneous emissions, in which the atomic ensemble collectively emits a photon following an atomic excitation. This serves an elementary mechanism to entangle the atomic states with discrete states of light, such as polarizations[7–9]. This bipartite entanglement can also be generated in the biphoton states in spatial modes, or energy-time[10], using means including parametric down conversion from nonlinear crystals[11,12], cascade emissions in atoms[13–16], or correlated light beams from a rare-earth ion-doped crystal[17].

To increase the efficiency of light-matter interaction, directional spontaneous emissions are enhanced in optically thick atomic ensembles[18–20] through superradiance[21,22], utilizing the resonant and pairwise dipole-dipole interactions[23,24] among the atoms in the dissipation process. This collective light-matter interaction also results in a frequency shift[25–33] and is responsible for subradiant radiations[34] as an afterglow of superradiance[35]. In the context of quantum memory, subradiant states are candidate systems for storing photons and can be actively prepared in a dense medium[36–41], through selective radiance by controlling the density and/or geometry of an array of atoms or metamolecules[42–44], collective antiresonances from the subradiant arrays in a cavity[45], or through creating quantum optical analogs of topological states in two-dimensional atomic arrays[46]. The light scattering from the subradiant states is also under active investigations recently[20,34], but a systematic and detailed study on the subradiant modes, which is essential for efficient assess to those modes, is still lacking.

The rapid development on precisely positioning single atoms utilizing photonic crystal waveguide[47], optical microtraps[48,49], or creating an array of artificial atoms in solid-state nanophotonic platforms[50] has further enabled fabrication of atomic ensembles with arbitrary spatial distributions beyond the diffraction limit of the excitation field, thus offers new opportunities to explore super- and subradiant modes, and opens up a new avenue for tailoring and modifying the quantum states of light and matter. In this paper, we propose to prepare the phase-imprinted single-photon subradiant states in the stacked ring arrays of atoms, in which light with orbital angular momentum (OAM)[51–55] interacts with the atoms, and the helical-phase-imprinted (HPI) subradiant states can be prepared upon absorption. The HPI subradiant states thus serves as good candidates for storing

[1]Institute of Physics, Academia Sinica, Taipei, 11529, Taiwan. [2]Institute of Atomic and Molecular Sciences, Academia Sinica, Taipei, 10617, Taiwan. Correspondence and requests for materials should be addressed to H.H.J. (email: sappyjen@gmail.com)

light quanta with OAM[56–58]. We investigate the light scattering out of these subradiant states for the cases of a few atoms, a single ring, and stacked rings. We also study the effect of uniform and spatially-dependent light polarizations on the scattering patterns.

Helical-Phase-Imprinted Subradiant States

When a near-resonant single photon is absorbed by an ensemble of N two-level atoms, a symmetric state is formed,

$$|\Phi_N\rangle = \frac{1}{\sqrt{N}} \sum_{\mu=1}^{N} e^{i\mathbf{k}_L \cdot \mathbf{r}_\mu} |e\rangle_\mu |g\rangle^{\otimes(N-1)},$$

(1)

where $|g\rangle$ and $|e\rangle$ label the ground and excited states of a two-level atom, and $\mathbf{k}_L$ is the wave vector of the plane-wave excitation field. Here, each of the two-level atoms can be promoted to the excited state with an equal probability N^{-1} and acquires a position-dependent traveling phase $e^{i\mathbf{k}_L \cdot \mathbf{r}_\mu}$. This symmetric state can be superradiant when the inter-atomic distance is much less than the resonant wavelength λ_a. Since the complete Hilbert space of single excitation involves N possible constructions of the bare states $|e\rangle_\mu |g\rangle^{\otimes(N-1)} \equiv |\psi_\mu\rangle$, then the remaining $N-1$ nonsymmetric states can be either super- or subradiant, depending on the atomic distributions. To systematically study and access those states, we have considered to use a phase-imprinting method[37,38,41] on a one-dimensional atomic array, which prepares the system into a De Moivre state:

$$|\Phi_m\rangle = \frac{1}{\sqrt{N}} \sum_{\mu=1}^{N} e^{i\mathbf{k}_L \cdot \mathbf{r}_\mu} e^{i\frac{2m\pi}{N}(\mu-1)} |\psi_\mu\rangle,$$

(2)

with $m \in [1, N]$, whose orthogonality is guaranteed by De Moivre's theorem. This phase imprinting method dynamically controls the linearly increased atomic phases either by a gradient Zeeman field or a gradient Stark field pulse. We note that the form of De Moivre states in equation (2) with $\mathbf{r}_\mu \to 0$ is first constructed in the degenerate subspace of a small sample[59].

While this method is simple, practically it, however, demands a large field gradient or long interaction time when the atomic array is short and/or the inter-atomic separation is small. Alternatively, by deforming the atomic array into a ring, this linearly increasing phase can be easily and exactly imprinted by light with a quantized orbital angular momentum (OAM). Thus, we consider a Laguerre-Gaussian (LG) beam in the paraxial approximation[60–62],

$$U_p^l(r, \phi, z) = \frac{C\hat{\varepsilon}}{w(z)} \left(\frac{\sqrt{2}\,r}{w(z)}\right)^{|l|} L_p^{|l|}\left(\frac{2r^2}{w^2(z)}\right) e^{-[r/w(z)]^2 - il\phi} e^{-ik_L z + i\psi(z) - ik_L r^2/[2R(z)]},$$

(3)

where $\hat{\varepsilon}$ denotes the polarization, $w(z) = w_0\sqrt{1 + (z/z_R)^2}$ is Gaussian beam width with the beam waist w_0, and $z_R = \pi w_0^2/\lambda$ is Rayleigh range. We denote the normalization constant as C, and $L_p^{|l|}$ is the associated Laguerre polynomials with radial mode numbers p. The Guoy phase is $\psi(z) = (2p + |l| + 1)\tan^{-1}(z/z_R)$ and the radius of curvature is $R(z) = z[1 + (z_R/z)^2]$. This paraxial approximation of LG beams is valid when $f = \lambda/(2\pi w_0) \ll 1$, and therefore, the spatially varying Guoy phase and $[e^{-ik_L r^2/[2R(z)]}]$ of the wavefront vanish respectively at $z = 0$ and infinite $R(z = 0)$. Under this circumstance, the HPI states can be prepared with a phase of $e^{il\phi}$ along the azimuthal direction. In our preparation scheme of various ring structures, we choose excitation photons with LG modes with $p = 0$ and assume they uniformly excite the atoms on absorption, similar to the timed Dicke state preparation[63]. We denote LG modes with zero radial index ($p = 0$) as

$$u_{p=0}^l(r, \phi) = \frac{C\hat{\varepsilon}}{w_0} \left(\frac{\sqrt{2}\,r}{w_0}\right)^{|l|} e^{-[r/w_0]^2 - il\phi},$$

(4)

where we have replaced $L_{p=0}^{|l|}(x) = 1$ for arbitrary x.

For N atoms sitting on a single ring with a constant separation between their nearest neighbors, the light propagating along the axis of the ring imprints the phase of $\phi = 2\pi l(\mu-1)/N$ on the atoms. A u_0^l photon absorbed by the ring array thus forms exactly the state of $|\Phi_{m=l}\rangle$ in equation (2). In Fig. 1, we show two stacked rings for an illustration of preparing such helical-phase-imprinted (HPI) states with a u_0^l photon, and the far-field observation of these states. For the multiply-stacked rings along $\hat{z}$, HPI states in general can be expressed as

$$|\Phi_l\rangle_{\text{HPI}} = \frac{1}{\sqrt{N}} \sum_{\mu_z=1}^{N_z} \sum_{\mu_\phi=1}^{N_\phi} e^{i\mathbf{k}_L \cdot \mathbf{r}_\mu} e^{i\frac{2l\pi}{N_\phi}(\mu_\phi-1)} |\psi_\mu\rangle,$$

(5)

where $N = N_z N_\phi$ for a number of N_z stacked rings, with N_ϕ atoms in each ring. The atomic position index μ is implicitly $(\mu_z - 1)N_\phi + \mu_\phi$, which labels the traveling phase by the excitation field on $|\psi_\mu\rangle$. The multiply-stacked rings allow a larger optical depth and stronger light-matter interactions, and thus increase the absorption efficiency. For the stacked rings along $\hat{r}$, forming a concentric structure in a two-dimensional plane, we can substitute N_z and μ_z with N_r and μ_r respectively in equation (5).

Below we investigate the emission patterns of HPI subradiant states, assuming they are excited and prepared genuinely. The efficiency, on the other hand, can be enhanced by using heralded single photon source or post
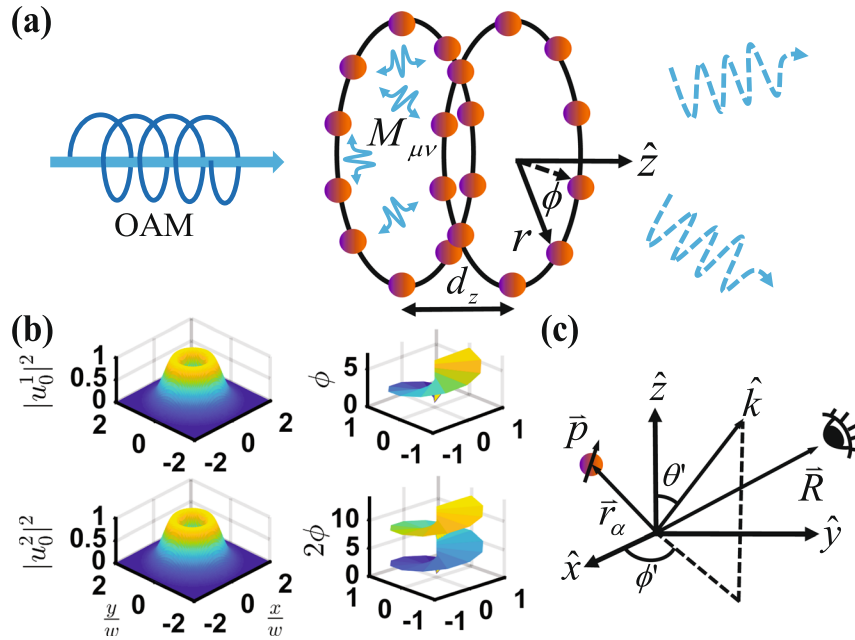
Figure 1. Schematic helical-phase-imprinted state preparation and far-field detection. (**a**) A single-photon source with orbital angular momentum (OAM) is absorbed by the atoms sitting on the stacked rings along $\hat{z}$ (two ring arrays are shown here for illustration). The atomic system is then prepared into one of the super- or subradiant states, depending on OAM of light. In the process of spontaneous decay, the resonant dipole-dipole interaction $M_{\mu\nu}$ couples μ^{th} and ν^{th} atoms on the stacked rings, and scatters the light collectively depending on the ring geometry of radius r, ϕ, and inter-ring distance d_z. (**b**) Typical light intensity (normalized) with OAM of Laguerre-Gaussian modes $u_0^l(r, \phi)$ and associated helical phases $e^{il\phi}$, for some beam waist radius w. (**c**) A far-field observer at $\vec{R}$ sees the scattered light from a dipole $\vec{p}$ at $\vec{r_\alpha}$ in 4π solid angle of mode $\hat{k}$ characterized by θ' and ϕ'.

selections. We note that non-perfect technical issues, such as nonparaxial conditions and the nonuniform spatial profile of an LG beam for multiply-stacked rings, compromise either the fidelity or efficiency of HPI state preparation, but can still be optimized by, for instance, using beams with a longer Rayleigh range or equivalently larger beam waist and by optimizing the alignment[64].

Light Scattering from HPI Subradiant States

In this section, we consider the resonant dipole-dipole interaction present in the dissipation of HPI states. This long-range interaction[23,24] arises from rescattering photons between atoms in the spontaneous emissions, and is the mechanism for superradiance or subradiance when atoms are close to each other. The explicit forms of the interaction and the far-field emission patterns of HPI states are derived in Methods respectively. Below we investigate the emission patterns for various atomic ring structures. We note that the angular distributions of the superradiant states have been recently investigated in linear chains[65–68].

Two-atom case. We first analyze the case of two atoms sitting on a ring with a radius r and excited by single photon carrying an OAM, $l\hbar$. Define the far-field scattering intensity $\Omega_l(\theta, \phi) \equiv \langle \vec{E}^*(\mathbf{R}, t) \vec{E}(\mathbf{R}, t) \rangle_l / I_0(t)$, we use equation (17) in Methods for two atoms on the x-axis with an $\hat{x}$ polarized excitation, and we obtain

$$\Omega_l(\theta, \phi) = (1 - \sin^2\theta \cos^2\phi)[2 + 2\cos(2|\mathbf{k}_L|r\sin\theta\cos\phi + l\pi)], \quad (6)$$

which corresponds to the case shown in Fig. 2(a), where two atoms are aligned parallel to the polarization of the excitation field. For the case where two atoms are aligned perpendicular to the polarization which is shown in Fig. 2(b), the factor in equation (6), $1 - \sin^2\theta\cos^2\phi$, is replaced by $\sin^2\theta\sin^2\phi$. Note that $|\mathbf{k}_R| = |\mathbf{k}_L|$, and different light polarizations result in different coupling strengths in equations (11) and (12) of Methods, and thus $I_0(t)$, due to different eigenvalues λ_m (see Methods). When $r \to 0$, $\Omega_l(\theta, \phi) \propto [1 + (-1)^l]$, which indicates that the excitation beam with odd OAM is not scattered at all in this extreme limit. According to equation (5), this specific HPI state is given as

$$|\Phi_l\rangle_{\text{HPI}} = \frac{1}{\sqrt{2}}(e^{i\mathbf{k}_L \cdot \mathbf{r}_1}|\psi_1\rangle + e^{i\mathbf{k}_L \cdot \mathbf{r}_2}e^{il\pi}|\psi_2\rangle), \quad (7)$$

which is a superradiant (subradiant) state for even (odd) l. The superradiant intensity for single photon scattering in the forward direction has a maximal $\Omega_l(\theta = 0) = 2$ which is proportional to $N^2/2$, as that in the half-excited spin models[21]. For single spin excitation in the N spin-1/2 model, the photon emission intensity is proportional
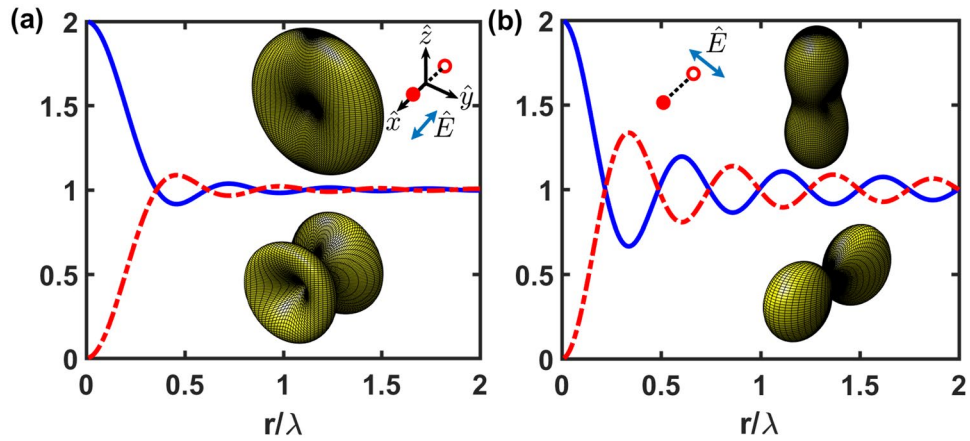
Figure 2. Eigenvalues and far-field property $\Omega_l(\theta, \phi)$ for two atoms sitting on the $\hat{x}$ axis. We show the real part of the rescaled eigenvalues, $-\lambda_{1,2}/(\Gamma/2)$, in the case of two atoms separating by $2r$, for the eigenstates of $l = 1$ (red dashed line, subradiant) and 2 (blue solid line, superradiant) with (**a**) $\hat{x}$ and (**b**) $\hat{y}$ polarized light excitations $\hat{E}$. Specific three-dimensional plots of $\Omega_l(\theta, \phi)$ at $r/\lambda = 0.15$ for the super- and subradiant states are illustrated respectively in the upper and lower parts of the graphs. Empty and filled circles indicate the ground and excited atoms, one of the bare states $|\psi_\mu\rangle$. The fitted exponential decay rates (in units of $\Gamma/2$) for super- and subradiant states are $\Gamma_f =$ (a) 1.5 and 0.51, (b) 1.1 and 0.9, respectively.

to $(l_m + m)(l_m - m + 1) = N$ in the Dicke's eigenstates with a total quantized angular momentum $l_m \hbar = N \hbar/2$ and magnetization $m \equiv (N_\uparrow - N_\downarrow)/2 = 1 - N/2$[21].

In Fig. 2, we show the eigenvalues and far-field property $\Omega_l(\theta, \phi)$ for two atoms separating by $2r$. The eigenvalues can be solved analytically from the coupling matrix $\hat{M}$ introduced in Methods, which are

$$\lambda_{1,2} = -\frac{\Gamma}{2} \pm \left[\frac{F_{12}(\xi) - i2G_{12}(\xi)}{2} \right],$$

(8)

where Γ is the natural decay rate (linewidth) of the excited-ground transition, and $\xi = 2|\mathbf{k}_L|r$. The rescaled real part of the eigenvalues in Fig. 2, which are decay constants, approach 2 and 0 as $r \to 0$, representing the super- and subradiant modes of the radiation. For larger r, the eigenvalues asymptotically converge to 1, corresponding to the regime of non-interacting (independent) emitters. Specific far-field property is chosen at $\xi = 0.3\pi$, which shows a forward-backward scattering along the excitation propagation direction, $\hat{z}$, and a transverse scattering for the super- ($l = 2$) and subradiant ($l = 1$) modes, respectively. Note that the $\hat{x}$ and $\hat{y}$ polarized excitations correspond to the head-to-tail and parallel polarization configurations, respectively, and the former (latter) suppresses light scattering in the $\hat{x}$ ($\hat{y}$) direction, which can be seen from equation (6) that the scattered light vanishes at $\theta = \pi/2$ and $\phi = 0$ ($\pi/2$). The head-to-tail polarizations also allow strong scattering in the superradiant mode in the direction transverse to the polarization orientation. On the contrary, with the parallel polarizations, the collective scattering rate along the $\hat{x}$ axis is suppressed to ~ 0.35 times the maximum scattering rate. This reflects the destructive interference of parallel polarized (virtual) photons from two atoms, which diminishes as $r \to 0$, where $\Omega_l(\theta, \phi)$ of these two polarization configurations restores the rotational symmetry of the superradiance case in Fig. 2(a), by taking $\phi \to \phi + \pi/2$.

The subradiant modes, on the contrary, preserve the scattering patterns in Fig. 2 at $r/\lambda \lesssim 0.35$ and 0.25 for head-to-tail and parallel polarizations respectively. This range of r can be estimated by $2|\mathbf{k}_L|r \sin\theta \cos\phi \approx \pi/2$ in equation (6), which indicates the phase slip of half of $l\pi$ ($l = 1$ for the subradiant mode). The angles can be chosen as $\theta = \pi/4$ ($\pi/2$) and $\phi = 0$ at the maximal scattering of the head-to-tail (parallel) polarizations in the small r limit. This estimation also reflects on the qualitative changes of the eigenvalues in Fig. 2, which start to oscillate around $\lambda_{1,2} = -\Gamma/2$. As r increases and passes the estimated range of 0.35λ or 0.25λ, a scattering transverse to forward/backward direction also appears in the superradiant modes, and the directionality of them disappears. In the range of $2r \gtrsim \lambda$, the clear phenomena of super- and subradiance disappear.

Single ring. For the geometry of N atoms sitting on a single ring with equal arc lengths, it is equivalent to an N-sided regular polygon. When $N \gg 1$, the far-field scattering pattern from atoms forming a regular polygon approaches that of a ring. Before we investigate the scattering of the many-body subradiant states in a single ring with a large N, we first study the case of three and four atoms, which form regular triangle and square respectively.

In Fig. 3(a,b), we show the far-field scattering of the HPI states, $\Omega_l(\theta, \phi)$'s with $l = 1-3$, for three atoms which are in a regular-triangle configuration and are excited by $\hat{x}$ and $\hat{y}$ polarized light, respectively. As expected, the superradiant modes for both polarizations, corresponding to $l = 3$, show directional forward-backward scatterings along $\hat{z}$. In contrast, for the subradiant modes with $l = 1$ and 2, the forward-backward scatterings are suppressed, and
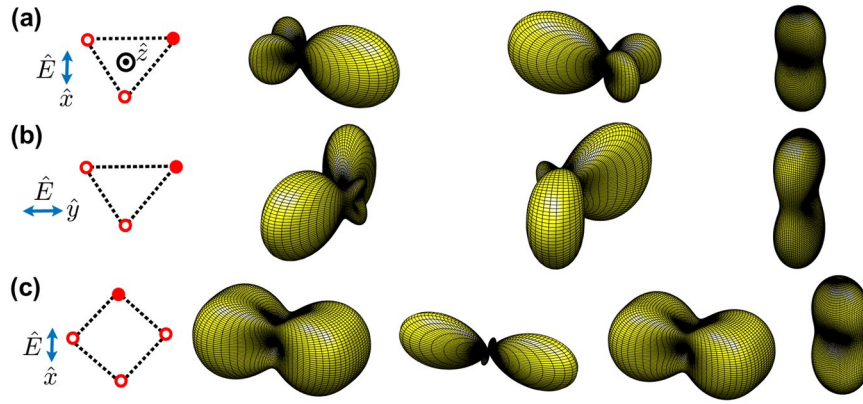
Figure 3. The far-field $\Omega_l(\theta, \phi)$ for three and four atoms sitting on a single ring. The atoms in top view form an (**a**) $\hat{x}$ and (**b**) $\hat{y}$ polarized triangular, and (**c**) $\hat{x}$ polarized square structures with the modes of $l = 1 - N$ respectively, where we choose $r/\lambda = 0.2$. Subradiant modes ($l = 1$ to $N - 1$) and superradiant modes ($l = N$) show directional transversal and forward-backward scatterings respectively. Note that $\Omega_l(\theta, \phi)$ of $\hat{y}$ polarized square preserves the C_4 rotational symmetry to the case of (**c**), and the viewing angles are the same as Fig. 2. Again empty and filled circles represent the ground and excited atoms, which displays one of the bare states $|\psi_\mu\rangle$. The fitted exponential decay rates for three- and four-atom rings (in units of $\Gamma/2$) are, $\Gamma_f =$ (**a**) 0.72, 0.72, 1.9, (**b**) 0.7, 0.7, 1.9, (**c**) 0.75, 0.13, 0.75, and 2.51 respectively.
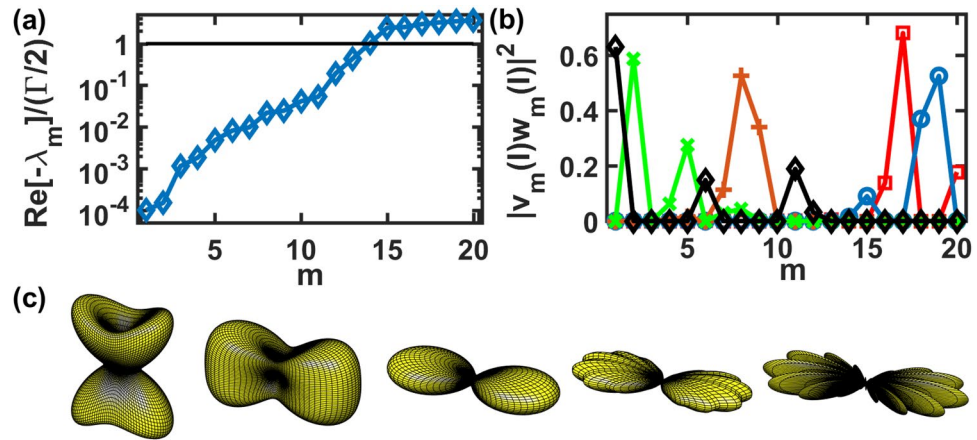

Figure 4. The decay rates, normalized weightings, and $\Omega_l(\theta, \phi)$ of a single ring with $N = 20$ and $r/\lambda = 0.5$. (**a**) The spontaneous decay rates shown in ascending order and logarithmic scale, which are derived from the real part of the eigenvalues λ_m. (**b**) The normalized weightings on the eigenmodes for $l = 1, 2, 5, 9$, and 10 ($\bigcirc$, $\square$, $+$, $\times$, and $\Diamond$ respectively), and (**c**) the corresponding $\Omega_l(\theta, \phi)$ (left to right), in the same viewing angle of Fig. 2. The fitted exponential decay rates for $l = 1, 2, 5, 9$, and 10 (in units of $\Gamma/2$), $\Gamma_f = 5.43, 4.77, 0.024, 1.3 \times 10^{-3}$, and 5×10^{-4}, respectively.

light is preferentially emitted into directions perpendicular to both k vector and the polarization of the incoming photon, which makes the $\hat{x} - \hat{z}$ and $\hat{y} - \hat{z}$ planes the nodal planes of Ω_l's for $\hat{x}$ and $\hat{y}$ excitations, respectively.

In Fig. 3(c), we study the case with four atoms forming a square. The $l = 2$ subradiant mode, possessing the lowest decay rate, is more directional than the modes with $l = 1$ and 3 which have the same $\Omega_l(\theta, \phi)$. Furthermore, in this specific structure, two perpendicularly excited polarizations result in the same pattern of the far-field scattering which preserves the C_4 rotational symmetry in ϕ. This C_4 symmetry also applies to all the number of atoms $N = 4n$ with integers n. We note that the far-field scatterings of the $l = 1$ and 3 modes are the same due to the symmetry of $l \to -l$, which will be further explained in Methods.

For many atoms on a single ring, we use $N = 20$ as an example and show the calculation results in Fig. 4. In this configuration, C_4 rotational symmetry sustains, and therefore, $\Omega_l(\theta, \phi)$ are the same for two linear polarizations. Figure 4(a) shows the calculated eigenmodes, with 14 subradiant and 6 superradiant modes, as the 14th mode is just below the line of $\lambda_m = -\Gamma/2$. The lowest subradiant eigenmode is 10^{-4} times the natural decay rate for $r/\lambda = 0.5$, which can be further reduced as r decreases. We selectively plot several representative HPI states in Fig. 4(b), in which each only occupies a few eigenmodes with significant weightings. It is seen that HPI states with $l = 1$ and 2 are superradiant, while that with $l = 5, 9$, and 10 are subradiant. In Fig. 4(c), the $\Omega_l(\theta, \phi)$ is plotted accordingly for the selected modes in 4(b). Except for the symmetric superradiant state of $l = N$, which has a clear
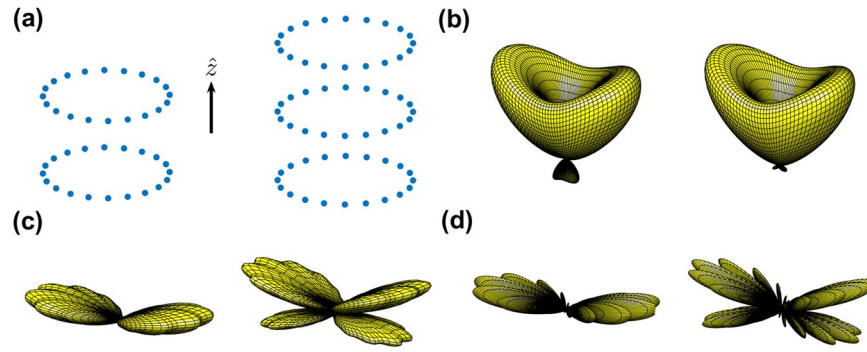
Figure 5. Schematics of $\hat{z}$-stacked ring arrays and their far-field properties $\Omega_l(\theta, \phi)$, with $r/\lambda = 0.5$. For the stacked ring arrays with $N_\phi = 20$ in (**a**), $\Omega_l(\theta, \phi)$'s of the HPI states of two and three $\hat{z}$-stacked rings with $d_z/\lambda = 0.35$ are illustrated for (**b**) $l = 1$ (superradiant), (**c**) $l = 9$ (subradiant), (**d**) $l = 10$ (subradiant), which exhibit enhancement on the forward scattering as the number of rings increases. The viewing angles are the same as Fig. 2.

forward-backward scattering similar to the previous cases of few atoms, the other superradiant modes, e.g., with $l = 1$ and 2, also show an oblique and transverse scatterings respectively. As l increases toward the most subradiant modes ($l = 10$), a clear side scattering at the right angles emerges, and this most subradiant HPI state further breaks $\Omega_l(\theta, \phi)$ into 10 concentric and flat lobes, each with a good directionality.

We note that $\Omega_l(\theta, \phi) = \Omega_{-l}(\theta, \phi) = \Omega_{N-l}(\theta, \phi)$ for even number of the atoms, which is also true for odd number of atoms at $r = 0$. For small r, $\Omega_l(\theta, \phi)$ of can be approximately reduced to the sum of imprinted helical phases $e^{i2l\pi(\beta_\phi - \alpha_\phi)/N_\phi}$. This gives in general a sum of cosine functions without the detail spatial phases from the atomic distributions of $\mathbf{r}_{\alpha\beta}$; therefore, $\Omega_l(\theta, \phi)$ is the same for lth and $(N-l)$th HPI states. For a finite r, only even number of the atoms N sustains the symmetry of $l \to -l$ in $\Omega_l(\theta, \phi)$. This can be seen from the pairwise and spatial phase contributions of $\mathbf{k}_R \cdot \mathbf{r}_{\alpha\beta}$, and we explain in more details in Methods.

Stacked rings. Atomic rings can be put into stacked configurations to further enhance the cooperative effects. In the following, we investigate $\hat{z}$- and planer concentric-stacking (referred as $\hat{r}$-stacking here), in which the assemblies are integrated along either the axial or the radial directions, respectively. Figure 5(a) shows schematically two and three $\hat{z}$-stacking rings, in which the inter-ring distance is characterized by the parameter d_z. For the HPI superradiant mode with $l = 1$, as in Fig. 5(b), the forward scattering is enhanced as number of rings increases, which breaks the symmetry of forward-backward scattering in Fig. 4(c). For the subradiant mode in Fig. 5(c,d), an oblique scattering toward the forward direction is enhanced as more atoms are integrated along the $\hat{z}$ direction. As we stack up more rings, the transverse scattering at $\theta = \pi/2$ in Fig. 4(c) can reappear as well. Therefore, the far-field scattering pattern can be greatly tuned by varying r, d_z ($\lesssim \lambda$), and the number of the stacked rings, which controls the intra- and inter-ring phase interferences.

In Fig. 6, we study the HPI states of s $\hat{r}$-stacking rings with $l = 1$ (superradiant), $l = 5$ (sub- and superradiant for $s < 3$), and $l = 9$ (subradiant for $s < 3$; sub- and superradiant for $4 < s < 6$). In this configuration, the inter-ring distance is characterized by d_r. Compared to the super- and subradiant modes in a single ring shown in Fig. 4(c), we find narrowing effects on $\Omega_l(\theta, \phi)$ for both θ and ϕ directions. For the $l = 1$ mode shown in Fig. 6(b), as the number of rings s is increased, far-field radiation is elongated toward forward and backward directions with narrower distributions in θ for each lobe. For $l = 5$ mode which is shown in Fig. 6(b), with the core-ring radius $r_c = 0.5\lambda$, inter-ring distance $d_r = r_c$, and the number of rings $s = 3$, $\Omega_l(\theta, \phi)$ splits into two lobes, bending toward forward and backward directions, similar to that in Fig. 6(a). This drastic change of scattering directions also accompanies with a crossover from sub- to superradiance. For the subradiant modes with $l = 9$ in Fig. 6(c), we also see localization of scattering in ϕ direction as s increases to 3, with the number of narrow lobes equal to $N_\phi = 20$. For $s = 4$ in Fig. 6(c), we see a noticeable broadening in θ direction, which again exhibits a crossover from the sub- to the superradiance. The mode at $s = 6$ becomes strong superradiant, but in contrast to the case of $l = N_\phi$ (equivalent to $l = 0$) which exhibits simply forward and backward scattering along $\hat{z}$, it further breaks the continuous symmetry in the ϕ direction and lead to 20 narrow superradiant lobes. Similar behaviors are seen in superradiant modes with $l = 8$. We note that the equivalence of maximum number of narrowed superradiant lobes and the number of atoms on each ring for a large $l \lesssim N_\phi/2$ ($l = 8, 9, 10$) is also a signature of the HPI states of $\hat{r}$-stacking rings. In contrast, for the $\hat{z}$-stacking rings, this feature only appears in the case with $l = N_\phi/2$, as shown in Figs 4(c) and 5(c).

Circular polarization. For the HPI states excited with circular polarization, $[(\hat{x} \pm i\hat{y})/\sqrt{2}]$, we expect more symmetric scattering patterns than with linear polarizations, and this is indeed the case as seen in Fig. 7. In this figure, we display the Ω_l's of the HPI subradiant states with $l = 1$ and 2 for few-atom cases, and that for many atoms with parameters adopted in a single ring structure in Fig. 4. For any uniform polarizations in general, $(\hat{\mathbf{R}} \cdot \hat{\mathbf{p}})^2$ in equation (17) can be replaced by $|\hat{\mathbf{R}} \cdot \hat{\mathbf{p}}|^2$, and as such, the handedness of the circular polarization does not matter to $\Omega_l(\theta, \phi)$. For the two-atom case, the scattering property can be derived by substituting the prefactor
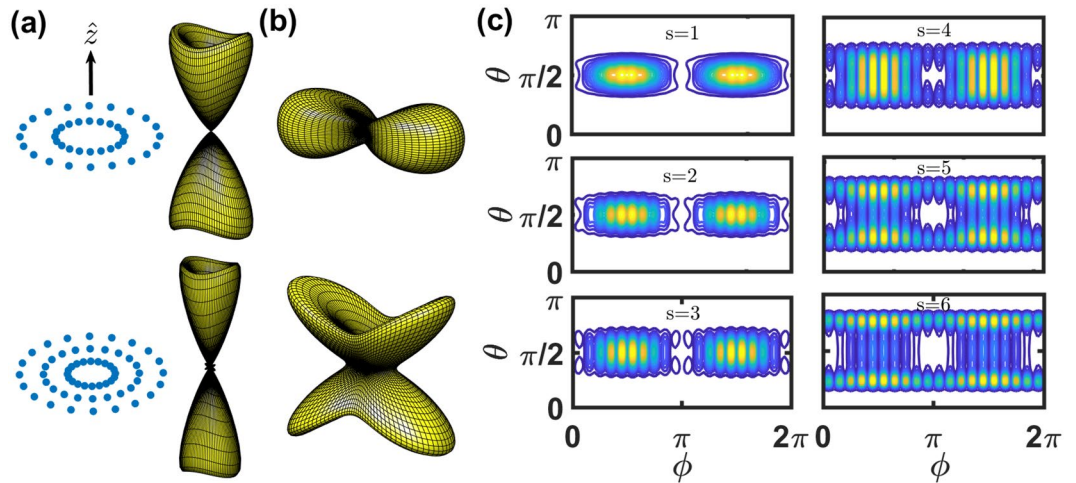
Figure 6. Schematics and the far-field scattering $\Omega_l(\theta, \phi)$ for s $\hat{r}$-stacked rings. (**a**) Schematic of $\hat{r}$-stacked rings with the Same N_ϕ as that in Fig. 5 in each ring, with equal inter-ring distance d_r. The $\Omega_l(\theta, \phi)$'s of the HPI states of two (upper) and three (lower) $\hat{r}$-stacked rings are illustrated for (**a**) $l = 1$ (superradiant), (**b**) $l = 5$ (sub- and superradiant for two and three rings respectively), and cross-sectional plots for (**c**) $l = 9$ (subradiant) excitations. The scattering intensity shows narrowing (localization) in polar angle θ for $l = 1$ modes while in both θ and ϕ for modes with $l = 9$ as number of rings increases. The splitting and further narrowing in θ for the states with $l = 9$, as seen in (**c**) for s from 1 to 6, indicating a crossover from the sub- to the superradiant modes. This crossover also appears in (**b**). The fitted exponential decay rates for $s = 1$–6 (in units of $\Gamma/2$), $\Gamma_f = 1.3 \times 10^{-3}$, 7.7×10^{-3}, 0.019, 1.4, 1.35, and 1.36, respectively.
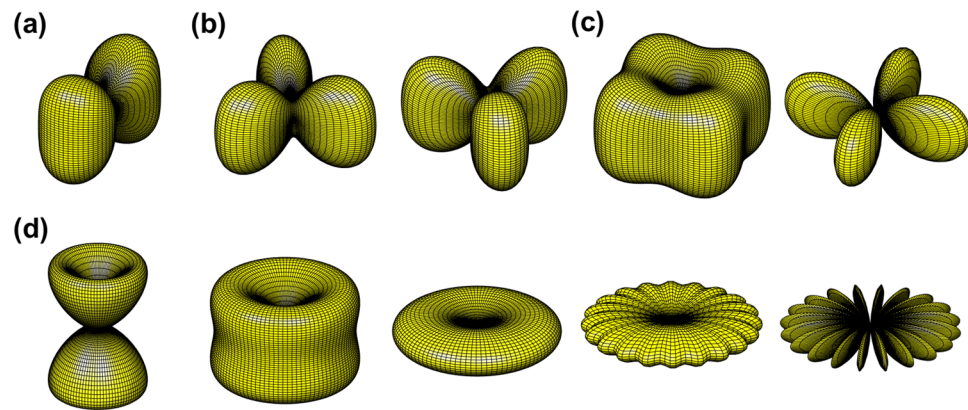

Figure 7. Far-field scattering from circularly polarized excitations. The Ω_l's of the HPI subradiant states are shown for (**a**) two-atom ($l = 1$), (**b**) three-atom ($l = 1$ and 2), and (**c**) four-atom cases ($l = 1$ and 2), at $r/\lambda = 0.2$. (**d**) The far-field scatterings of a single ring (same N and r for Fig. 4) with a circularly polarized excitation with $l = 1, 2, 5, 9$, and 10 are illustrated horizontally. The fitted exponential decay rates (in units of $\Gamma/2$), $\Gamma_f = $ (**a**) 0.7, (**b**) 0.57 for both modes, (**c**) 0.7, 0.11, (**d**) 4, 3.3, 0.018, 7×10^{-8}, and 3.5×10^{-9}, respectively.

of equation (6), $\sin^2\theta\cos^2\phi$, by $\sin^2\theta/2$. Similar to the case with linear polarizations in Fig. 2, scattering is suppressed on the $\hat{y} - \hat{z}$ plane but maximized on the $\hat{x} - \hat{z}$ plane, which can be identified in Fig. 7(a). This is exactly the sum of the far-field scattering of HPI state for two linear-polarizations with $l = = 1$ in Fig. 2. For three and four atoms, $\Omega_l(\theta, \phi)$ of the subradiant modes peak at discrete azimuthal angles $\phi = \phi_s + 2\pi/N$, preserving the C_N rotational symmetry for ϕ, where ϕ_s is the offset of the angle, depending on which subradiant mode we consider in Fig. 7(b,c).

For a single ring with $N = 20$ atoms, the HPI states go from super- to sub-radiant modes as l is increased, in which scattering in the forward/backward directions diminishes while the scattering in the transverse direction grows. For subradiant modes with $l = 9$ and 10, $\Omega_l(\theta, \phi)$ breaks into 20 radiation lobes with narrow distribution in ϕ. In contrast to the similar effect seen in Figs 4, 5 and 6, circular polarization gives higher azimuthal rotational symmetry. This rotational C_N symmetry also applies to the cases of $\hat{z}$- and $\hat{r}$-stacking rings in Fig. 5. In the $\hat{r}$-stacking configurations, narrowing effects in θ and ϕ also appear, similar to that in Fig. 6(c).

We note that in general, elliptically polarized light represents all possible uniform polarizations of field excitations, and therefore, linear and circular polarizations are the special cases of elliptical ones. In terms of a
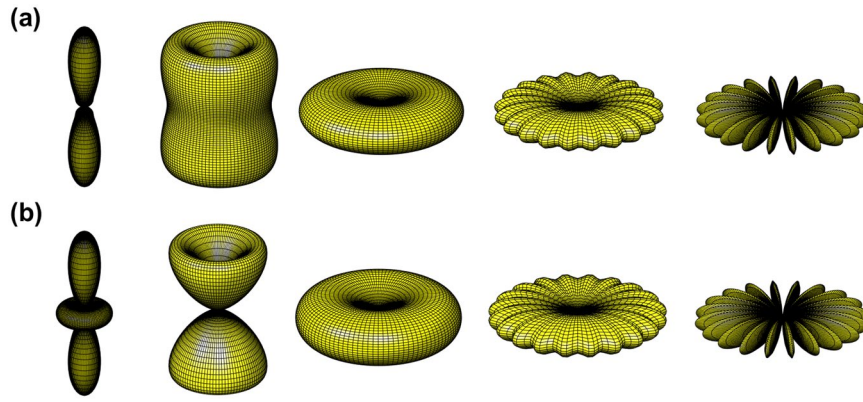
Figure 8. Far-field scattering from radially and azimuthally polarized excitations. The Ω_l's of the HPI super- and subradiant states are plotted for a single ring with the same N and r of Fig. 4, which are excited by (**a**) radial and (**b**) azimuthal polarizations. The modes of $l = 1, 2, 5, 9,$ and 10 are illustrated from left to right. The corresponding fitted decay rates for these modes (in units of $\Gamma/2$), $\Gamma_f =$ (**a**) 2.3, 3.5, 0.098, 1.2×10^{-6}, 7.4×10^{-8}, (**b**) 3.9, 1.6, 0.074, 1.1×10^{-6}, 6.9×10^{-8}, respectively.

normalized Jones vector, an elliptical polarization can be expressed as $(\cos\theta_a \hat{x} + \sin\theta_a e^{i\theta_e} \hat{y})$ where θ_a and θ_e are two angles to characterize the strengths and phases of the polarizations in $\hat{x} - \hat{y}$ plane. The vector of elliptical polarization traverses a rotated ellipse with an orientation angle α from the $\hat{x}$-axis determined by $\tan\alpha = \tan\theta_a \cos\theta_e$. Therefore, $(\theta_e = 0)$ and $(\theta_e = \pm\pi/2, \theta_a = \pi/4)$ correspond to linear and circular polarizations respectively. For other angles, elliptical polarizations should generate the emission patterns with unequal superpositions of $\hat{x}$- and $\hat{y}$-polarized cases. Here and in the previous section, we show the results of circular and linear polarizations only, which should be sufficient and representative.

Radial and azimuthal polarizations. Finally we study the scattering properties from the radially and azimuthally polarized excitations[64], which allows us to further manipulate the local orientations of the atomic dipoles. The resonant dipole-dipole interactions in equations (11) and (12) can be straightforwardly generalized by replacing the term $[1 - (\hat{\mathbf{p}} \cdot \hat{r}_{\mu\nu})^2]$ with $[(\hat{\mathbf{p}}_\beta^* \cdot \hat{\mathbf{p}}_\alpha) - (\hat{\mathbf{p}}_\beta^* \cdot \hat{r}_{\alpha\beta})(\hat{\mathbf{p}}_\alpha \cdot \hat{r}_{\alpha\beta})]$ and correspondingly the term $[1 - 3(\hat{\mathbf{p}} \cdot \hat{r}_{\mu\nu})^2]$ with $[(\hat{\mathbf{p}}_\beta^* \cdot \hat{\mathbf{p}}_\alpha) - 3(\hat{\mathbf{p}}_\beta^* \cdot \hat{r}_{\alpha\beta})(\hat{\mathbf{p}}_\alpha \cdot \hat{r}_{\alpha\beta})]$. Similarly, the far-field Ω_l of equation (17) can also be generalized by replacing $[1 - (\hat{\mathbf{R}} \cdot \hat{\mathbf{p}})^2]$ with $[(\hat{\mathbf{p}}_\beta^* \cdot \hat{\mathbf{p}}_\alpha) - (\hat{\mathbf{p}}_\beta^* \cdot \hat{\mathbf{R}})(\hat{\mathbf{p}}_\alpha \cdot \hat{\mathbf{R}})]$ and summing over indices α and β.

The polarizations for the radially and azimuthally excited atoms can be denoted as $\hat{\mathbf{p}}_\alpha = \hat{e}_r$ and $\hat{e}_\phi$ which are $[\cos\phi(\alpha)\hat{x} + \sin\phi(\alpha)\hat{y}]$ and $[-\sin\phi(\alpha)\hat{x} + \cos\phi(\alpha)\hat{y}]$ in Cartesian coordinates, respectively. The polarization rotates with an angle $\phi(\alpha) = 2\pi\alpha_\phi/N_\phi$ which will imprint on the atoms in addition to the OAM phase. Unlike the circular polarizations which have definite spin angular momentum $(\pm 1\hbar)$ in a photon, the radial and azimuthal polarizations can only relate to the circular ones by $\hat{e}_r \pm i\hat{e}_\phi = (\hat{x} \pm i\hat{y})e^{\mp i\phi}$. This indicates that an equal superposition with $\pm\pi/2$ phase shift between the radial and azimuthal polarizations of light is the same as the left (right)-handed circular polarization with one quanta shift $(\mp\hbar)$ of OAM. In Fig. 8, we demonstrate the far-field scattering patterns from radially and azimuthally polarized excitations. Both $l = 1$ HPI states exhibit the superradiant ($l = N_\phi$ or equivalently $l = 0$) scattering patterns with a signature of strong scattering into the forward and backward directions. As l increases, we find that the transverse far-field scattering patterns are enhanced while forward/backward directions are suppressed, similar to Fig. 7(d). When $l \approx N_\phi/2$, the corresponding HPI state is the most subradiant state, and Ω_l splits into N_ϕ thin slab-like radiation lobes. In this case, we find that all of the patterns from circularly, radially, or azimuthally polarized excitations approach to each other. This is due to both the symmetry of $l \rightarrow -l$ in $\Omega_l(\theta, \phi)$ and the discrete rotational symmetry C_N are satisfied. Similarly, the stacked rings along $\hat{z}$ or $\hat{r}$ respectively enhances the forward scattering and the narrowing effect as in Fig. 5 with again an additional C_N symmetry.

Discussion and Conclusion

In this paper, the requirement for preparing a photon carrying an OAM is relatively easy to fulfill, and a recent experiment showed that an OAM beam with as high as $10,000\hbar$ can be generated[69], thus suggests that our scheme is pragmatic with a scalability up to thousands of atoms. The requirement of reaching strong coupling, *viz.* the inter-atomic separation $d \lesssim 0.5\lambda$, is more stringent but can also be reached. For real atoms, it requires the atomic density comparable to that of an atomic Bose-Einstein condensate (BEC). As such, one can achieve by loading a BEC into a ring trap with a relatively tight radial confinement. On the other hand, it may be even more practical and promising to construct a strong-interacting ring with artificial atoms in solids[70,71], given the high controllability of the atomic positions nowadays. It is of the reach of current technology to fabricate and construct a ring with μm-sized superconducting devices driven by a microwave field of wavelength $\lambda > 500\,\mu$m or diamond color centers doped with 40-nm precision and driven by a near-infrared light at $\lambda = 750\,$nm[50]. Both systems allow strong resonant dipole-dipole interactions as $r/\lambda \sim 0.05$. For thermal atomic system[28,72,73], we can add position

fluctuations in our theory to simulate the effect of thermal fluctuations. We expect that the scattering patterns will be smoothed out and the fluctuation will suppress the lifetime[43] of the HPI subradiant states.

The scattered patterns $\Omega_l(\theta, \phi)$'s not only provide useful information for light collections but offers far-field scattering fingerprints that can be traced back to the atomic spatial distributions, as well as the polarizations, thus offers one to study light-matter interactions in greater details. For practical applications in quantum memory, as the far-field radiation patterns of the super- and sub-radiant HPI states are very different, one can efficiently collect the transversally scattered light from the subradiant states using a parabolic mirror with the forward and backward scattering blocked. While we have discussed stacking rings along the $\hat{z}$ and $\hat{r}$ directions in this study, there are many other interesting geometries which can be studied, such as atoms arranged in a cylindrical shell with a chirality or even in a torus-like shape, making our scheme a versatile platform for engineering the properties of the HPI many-body states and their emission patterns for quantum optical applications.

Finally, storing and manipulating quantum information using a light with a large OAM in principle allows massive entanglement, which is potentially useful in implementing high-dimensional quantum gates for quantum computation[74], as well as handling hyper-entangled photons which simultaneously entangle OAM and such as the polarization (spin) degrees of freedom, for higher information capacity[75].

Methods

Lindblad form of dissipation with resonant dipole-dipole interactions.
The theoretical analysis for the fluorescence and light scattering is based on the Lindblad forms of the spontaneous emissions. The general spontaneous emission process involves the long-range dipole-dipole interaction[23,24]. This pairwise interaction originates from the rescattering events in the common quantized light field. For an arbitrary quantum operator $\hat{Q}$, the Heisenberg equation in a Lindblad form gives

$$\frac{d\hat{Q}}{dt} = -i\sum_{\mu\neq\nu}^{N}\sum_{\nu=1}^{N} G_{\mu\nu}[\hat{Q}, \hat{\sigma}_\mu^+\hat{\sigma}_\nu^-] + \mathcal{S}_s[\hat{Q}],$$

(9)

where for the spontaneous emission,

$$\mathcal{S}_s[\hat{Q}] = -\sum_{\mu,\nu=1}^{N}\frac{F_{\mu\nu}}{2}\left(\hat{\sigma}_\mu^+\hat{\sigma}_\nu^-\hat{Q} + \hat{Q}\hat{\sigma}_\mu^+\hat{\sigma}_\nu^- - 2\hat{\sigma}_\mu^+\hat{Q}\hat{\sigma}_\nu^-\right).$$

(10)

The dipole operator is $\hat{\sigma}_\mu^-$ ($\hat{\sigma}_\mu^+$) where $\hat{\sigma}_\mu^- \equiv |g\rangle_\mu\langle e|$ and $\hat{\sigma}_\mu^- \equiv (\hat{\sigma}_\mu^+)^\dagger$. The pairwise frequency shift $G_{\mu\nu}$ and decay rate $F_{\mu\nu}$ are[24]

$$F_{\mu\nu}(\xi) \equiv \frac{3\Gamma}{2}\left\{\left[1 - (\hat{\mathbf{p}}\cdot\hat{r}_{\mu\nu})^2\right]\frac{\sin\xi}{\xi} + \left[1 - 3(\hat{\mathbf{p}}\cdot\hat{r}_{\mu\nu})^2\right]\left(\frac{\cos\xi}{\xi^2} - \frac{\sin\xi}{\xi^3}\right)\right\},$$

(11)

$$G_{\mu\nu}(\xi) \equiv \frac{3\Gamma}{4}\left\{-[1 - (\hat{\mathbf{p}}\cdot\hat{r}_{\mu\nu})^2]\frac{\cos\xi}{\xi} + [1 - 3(\hat{\mathbf{p}}\cdot\hat{r}_{\mu\nu})^2]\left(\frac{\sin\xi}{\xi^2} + \frac{\cos\xi}{\xi^3}\right)\right\},$$

(12)

where Γ is the single-particle natural decay rate of the excited state, $\xi = |\mathbf{k}_L|r_{\mu\nu}$, and the interparticle distance $r_{\mu\nu} = |\mathbf{r}_\mu - \mathbf{r}_\nu|$. The above expressions are valid for uniformly polarized excitations of the dipole orientations $\mathbf{p}$.

The time evolutions of the HPI states can be determined by the eigenvalues and eigenvectors of the coupling matrix $\hat{M}$ with $M_{\mu\nu} = (-F_{\mu\nu} + i2G_{\mu\nu}\delta_{\mu\neq\nu})e^{-i\mathbf{k}_L\cdot(\mathbf{r}_\mu-\mathbf{r}_\nu)}/2$ in the bare state bases $|\psi_\mu\rangle$. Denote the eigenvalues and eigenvectors as λ_m and $\hat{U}$ respectively, the time evolution of the HPI state $|\Psi(t)\rangle = h_l(t)|\Phi_l\rangle_{\mathrm{HPI}}$ reads[37,38,41]

$$h_l(t) = \sum_{m=1}^{N} v_m(l)e^{\lambda_m t}w_m(l),$$

(13)

$$v_m(l) = \sum_{\mu_z=1}^{N_z}\sum_{\mu_\phi=1}^{N_\phi}\frac{U_{\mu m}}{\sqrt{N}}e^{-i\frac{2l\pi}{N_\phi}(\mu_\phi-1)},$$

(14)

$$w_m(l) = \sum_{\nu_z=1}^{N_z}\sum_{\nu_\phi=1}^{N_\phi}\frac{U_{m\nu}^{-1}}{\sqrt{N}}e^{i\frac{2l\pi}{N_\phi}(\nu_\phi-1)},$$

(15)

where the atomic position index ν is implicitly $(\nu_z-1)N_\phi+\nu_\phi$, which is the same as μ. The eigen-spectrum of λ_m involves both super- and subradiant decay rates along with the associated frequency shifts, and $|v_m(l)|^2$ is essentially the fidelity of $|\Phi_l\rangle_{\mathrm{HPI}}$ to the mth eigenstate, while $|v_m(l)w_m(l)|^2$ gives a measure of how much λ_m contributes to the HPI state dynamics.

Far-field scattering.
The far-field scattering properties provide measurable information for characterizing the HPI states and the atomic system. Similar ring lattice has been used to prepare Rydberg states[76] which show collective effects in the photon emissions. Here we use the general expression of the far-field scattering from the two-level atoms in Heisenberg picture[24],

$$\langle \overrightarrow{E}^{*}(\mathbf{R},\, t')\overrightarrow{E}(\mathbf{R},\, t)\rangle = \left(\frac{\omega_{eg}^{2}}{4\pi\varepsilon_{0}c^{2}}\right)^{2}\frac{|\overrightarrow{p}|^{2}}{R^{2}}[1 - (\hat{\mathbf{R}}\cdot\hat{\mathbf{p}})^{2}]\sum_{\alpha,\beta=1}^{N}e^{i\mathbf{k}_{R}\cdot\mathbf{r}_{\alpha\beta}}\langle\hat{\sigma}_{\alpha}^{+}(t')\hat{\sigma}_{\beta}^{-}(t)\rangle, \tag{16}$$

where ω_{eg} is the energy difference, $R = |\mathbf{R}|$, $\mathbf{r}_{\alpha\beta} = \mathbf{r}_{\alpha} - \mathbf{r}_{\beta}$, and the orientation of the dipole moment $\overrightarrow{p}$ is determined by the polarization of the excitation. The far-field derivation assumes that the observation point is far compared to the size of the atomic ring, such that $\omega_{eg}|\mathbf{R} - \mathbf{r}_{\alpha}|/c \gg 1$. This also suggests that the radiation mode $\mathbf{k} \approx \mathbf{k}_{R}//\mathbf{R}_{\alpha}\;[=(\mathbf{R} - \mathbf{r}_{\alpha})]$ in Fig. 1 in the main paper, which indicates of the retarded phase $e^{ik_{R}(R_{\alpha} - R)} \approx e^{-i\mathbf{k}_{R}\cdot\mathbf{r}_{\alpha}}$. Similar and more general expression can also be derived for a four-level atomic system[77] (three Zeeman levels in the $J = 1$ excited state, as in strontium atoms), which takes equation (16) in a tensor form of dipole transitions.

Set the time $t = t'$ in equation (16), we can calculate the radiation field intensity in terms of the dipole operators in Schrödinger picture, that is, $\langle\Psi(t)|\hat{\sigma}_{\alpha}^{+}\hat{\sigma}_{\beta}^{-}|\Psi(t)\rangle$. Therefore, by substituting the HPI states $|\Psi(t)\rangle = h_{l}(t)|\Phi_{l}\rangle_{\text{HPI}}$, we obtain the radiation field intensity,

$$\frac{\langle\overrightarrow{E}^{*}(\mathbf{R},\, t)\overrightarrow{E}(\mathbf{R},\, t)\rangle_{l}}{I_{0}(t)} = [1 - (\hat{\mathbf{R}}\cdot\hat{\mathbf{p}})^{2}]\sum_{\alpha,\beta=1}^{N}e^{i(\mathbf{k}_{R}-\mathbf{k}_{L})\cdot\mathbf{r}_{\alpha\beta}}\frac{1}{N}e^{\frac{i2l\pi}{N_{\phi}}(\beta_{\phi}-\alpha_{\phi})}, \tag{17}$$

where $I_{0}(t) = I_{n}h_{l}^{*}(t)h_{l}(t)$ is the time-evolving fluorescence intensity with $I_{n} \equiv (\omega_{eg}|\overrightarrow{p}|)^{2}/(4\pi\varepsilon_{0}c^{2}R)^{2}$, and again $\alpha(\beta)$ has an implicit dependence of $\alpha_{\phi}(\beta_{\phi})$. Equation (17) characterizes the far-field scattering property from the HPI states prepared by an excitation field of lth OAM, which involves the interplay of the atomic distributions $\mathbf{r}_{\alpha\beta}$ and the imprinted phases $e^{i2l\pi/N_{\phi}}$.

Mode symmetry. The mode symmetry of $\Omega_{l}(\theta, \phi) = \Omega_{-l}(\theta, \phi) = \Omega_{N-l}(\theta, \phi)$ for even number of the atoms can be explained in a polygon geometry with the pairwise and spatial phase contributions of $\mathbf{k}_{R}\cdot\mathbf{r}_{\alpha\beta}$. These include a combination of C_{2}^{N} cosine functions with N nearest-neighbor components ($\beta = \alpha + 1$) and with $N(N-3)/2$ diagonals in the geometry of N-polygon. The nearest-neighbor components pair up and interchange with l and $-l$. For the diagonals, they can be further grouped into $(N/2 - 2)$ different lengths (next nearest-neighbor, next next nearest-neighbor, etc.) with N components respectively, and the diagonal with the maximal length $(2r)$ with $N/2$ components. Again the N components in the respective groups can be interchanged with l and $-l$. The $N/2$ components in the maximal diagonal go back to themselves as $l \rightarrow -l$. This is due to the form of $\cos(l\pi + \mathbf{k}_{R}\cdot\mathbf{r}_{\alpha\beta})$ which is the same as $\cos(-l\pi + \mathbf{k}_{R}\cdot\mathbf{r}_{\alpha\beta})$ with a phase difference of $2l\pi$.

References

1. Hammerer, K., Sørensen, A. S. & Polzik, E. S. Quantum interface between light and atomic ensembles. *Rev. Mod. Phys.* **82**, 1041 (2010).
2. Chanelière, T. *et al.* Quantum telecommunication based on atomic cascade transitions. *Phys. Rev. Lett.* **96**, 093604 (2006).
3. Radnaev, A. G. *et al.* A quantum memory with telecom-wavelength conversion. *Nat. Phys.* **6**, 894–899 (2010).
4. Jen, H. H. & Kennedy, T. A. B. Efficiency of light-frequency conversion in an atomic ensemble. *Phys. Rev. A* **82**, 023815 (2010).
5. Kimble, H. J. The quantum internet. *Nature* **453**, 1023–1030 (2008).
6. Duan, L.-M., Lukin, M. D., Cirac, J. I. & Zoller, P. Long-distance quantum communication with atomic ensembles and linear optics. *Nature* **414**, 413–418 (2001).
7. Clauser, J. F., Horne, M. A., Shimony, A. & Holt, R. A. Proposed experiment to test local hidden-variable theories. *Phys. Rev. Lett.* **23**, 880–884 (1969).
8. Aspect, A., Grangier, P. & Roger, G. Experimental tests of realistic local theories via Bell's theorem. *Phys. Rev. Lett.* **47**, 460–463 (1981).
9. Kwiat, P. G. *et al.* New high-intensity source of polarization-entangled photon pairs. *Phys. Rev Lett.* **75**, 4337–4341 (1995).
10. Braunstein, S. L. & van Loock, P. Quantum information with continuous variables. *Rev. Mod. Phys.* **77**, 513–577 (2005).
11. Law, C. K., Walmsley, I. A. & Eberly, J. H. Continuous frequency entanglement: Effective finite Hilbert space and entropy control. *Phys. Rev. Lett.* **84**, 5304–5307 (2000).
12. Parker, S., Bose, S. & Plenio, M. B. Entanglement quantification and purification in continuous-variable systems. *Phys. Rev. A* **61**, 032305 (2000).
13. Jen, H. H. Spectral analysis for cascade-emission-based quantum communication in atomic ensembles. *J. Phys. B: At. Mol. Opt. Phys.* **45**, 165504 (2012).
14. Jen, H. H. & Chen, Y.-C. Spectral shaping of cascade emissions from multiplexed cold atomic ensembles. *Phys. Rev. A* **93**, 013811 (2016).
15. Jen, H. H. Entropy of entanglement in the continuous frequency space of the biphoton state from multiplexed cold atomic ensembles. *J. Phys. B: At. Mol. Opt. Phys.* **49**, 035503 (2016).
16. Jen, H. H. Cascaded cold atomic ensembles in a diamond configuration as a spectrally entangled multiphoton source. *Phys. Rev. A* **95**, 043840 (2017).
17. Li, C. *et al.* Controlled Correlation and Squeezing in Pr^{3+}:Y$_2$SiO$_5$ to Yield Correlated Light Beams. *Phys. Rev. Applied* **7**, 014023 (2017).
18. Bromley, S. L. *et al.* Collective atomic scattering and motional effects in a dense coherent medium. *Nat. Commun.* **7**, 11039 (2016).
19. Zhu, B., Cooper, J., Ye, J. & Rey, A. M. Light scattering from dense cold atomic media. *Phys. Rev. A* **94**, 023612 (2016).
20. Shahmoon, E., Wild, D. S., Lukin, M. D. & Yelin, S. F. Cooperative resonances in light scattering from two-dimensional atomic arrays. *Phys. Rev. Lett.* **118**, 113601 (2017).
21. Dicke, R. H. Coherence in spontaneous radiation processes. *Phys. Rev.* **93**, 99–110 (1954).
22. Gross, M. & Haroche, S. Superradiance: An essay on the theory of collective spontaneous emission. *Phys. Rep.* **93**, 301–396 (1982).
23. Stephen, M. J. First-order dispersion forces. *J. Chem. Phys.* **40**, 669–673 (1964).
24. Lehmberg, R. H. Radiation from an N-Atom System. I. General Formalism. *Phys. Rev. A* **2**, 883–888 (1970).
25. Friedberg, R., Hartmann, S. R. & Manassah, J. T. Frequency shifts in emission and absorption by resonant systems ot two-level atoms. *Phys. Rep.* **7**, 101–179 (1973).
26. Scully, M. O. Collective Lamb shift in single photon Dicke superradiance. *Phys. Rev. Lett.* **102**, 143601 (2009).

27. Röhlsberger, R., Schlage, K., Sahoo, B., Couet, S. & Rüffer, R. Collective Lamb shift in single-photon superradiance. *Science* **328**, 1248–1251 (2010).
28. Keaveney, J. *et al.* Cooperative Lamb shift in an atomic vapor layer of nanometer thickness. *Phys. Rev. Lett.* **108**, 173601 (2012).
29. Meir, Z., Schwartz, O., Shahmoon, E., Oron, D. & Ozeri, R. Cooperative Lamb Shift in a mesoscopic atomic array. *Phys. Rev. Lett.* **113**, 193002 (2014).
30. Pellegrino, J. *et al.* Observation of suppression of light scattering induced by dipole-dipole interactions in a cold-atom ensemble. *Phys. Rev. Lett.* **113**, 133602 (2014).
31. Jen, H. H. Superradiant cascade emissions in an atomic ensemble via four-wave mixing. *Ann. of Phys. (N.Y.)* **360**, 556–570 (2015).
32. Jennewein, S. *et al.* Coherent scattering of near-resonant light by a dense microscopic cold atomic cloud. *Phys. Rev. Lett.* **116**, 233601 (2016).
33. Jenkins, S. D. *et al.* Optical resonance shifts in the fluorescence of thermal and cold atomic gases. *Phys. Rev. Lett.* **116**, 183601 (2016).
34. Guerin, W., Araújo, M. O. & Kaiser, R. Subradiance in a large cloud of cold atoms. *Phys. Rev. Lett.* **116**, 083601 (2016).
35. Mazets, I. E. & Kurizki, G. Multiatom cooperative emission following single-photon absorption: Dicke-state dynamics. *J. Phys. B: At. Mol. Opt. Phys.* **40**, F105–F112 (2007).
36. Scully, M. O. Single photon subradiance: quantum control of spontaneous emission and ultrafast readout. *Phys. Rev. Lett.* **115**, 243602 (2015).
37. Jen, H. H., Chang, M.-S. & Chen, Y.-C. Cooperative single-photon subradiant states. *Phys. Rev. A* **94**, 013803 (2016).
38. Jen, H. H. Cooperative single-photon subradiant states in a three-dimensional atomic array. *Ann. Phys. (N. Y.)* **374**, 27–34 (2016).
39. Sutherland, R. T. & Robicheaux, F. Collective dipole-dipole interactions in an atomic array. *Phys. Rev. A* **94**, 013847 (2016).
40. Bettles, R. J., Gardiner, S. A. & Adams, C. S. Cooperative eigenmodes and scattering in one-dimensional atomic arrays. *Phys. Rev. A* **94**, 043844 (2016).
41. Jen, H. H. Phase-imprinted multiphoton subradiant states. *Phys. Rev. A* **96**, 023814 (2017).
42. Asenjo-Garcia, A., Moreno-Cardoner, M., Albrecht, A., Kimble, H. J. & Chang, D. E. Exponential improvement in photon storage fidelities using subradiance and "selective radiance" in atomic arrays. *Phys. Rev. X* **7**, 031024 (2017).
43. Facchinetti, G., Jenkins, S. D. & Ruostekoski, J. Storing light with subradiant correlations in arrays of atoms. *Phys. Rev. Lett.* **117**, 243601 (2016).
44. Jenkins, S. D., Ruostekoski, J., Papasimakis, N., Savo, S. & Zheludev, N. I. Many-body subradiant excitations in metamaterial arrays: Experiment and theory. *Phys. Rev. Lett.* **119**, 053901 (2017).
45. Plankensteiner, D., Sommer, C., Ritsch, H. & Genes, C. Cavity antiresonance spectroscopy of dipole coupled subradiant arrays. *Phys. Rev. Lett.* **119**, 093601 (2017).
46. Perczel, J. *et al.* Topological quantum optics in two-dimensional atomic arrays. *Phys. Rev. Lett.* **119**, 023603 (2017).
47. Goban, A. *et al.* Superradiance for atoms trapped along a photonic crystal waveguide. *Phys. Rev. Lett.* **115**, 063601 (2015).
48. Barredo, D., de Léséleuc, S., Lienhard, V., Lahaye, T. & Browaeys, A. An atom-by-atom assembler of defect-free arbitrary two-dimensional atomic arrays. *Science* **354**, 1021–1023 (2016).
49. Endres, M. *et al.* Atom-by-atom assembly of defect-free one-dimensional cold atom arrays. *Science* **354**, 1024–1027 (2016).
50. Sipahigil, A. *et al.* An integrated diamond nanophotonics platform for quantum-optical networks. *Science* **354**, 847–850 (2016).
51. Arnaut, H. H. & Barbosa, G. A. Orbital and intrinsic angular momentum of single photons and entangled pairs of photons generated by parametric down-conversion. *Phys. Rev. Lett.* **85**, 286 (2000).
52. Mair, A., Vaziri, A., Weihs, G. & Zeilinger, A. Entanglement of Orbital Angular Momentum States of Photons. *Nature* **412**, 313–316 (2001).
53. Molina-Terriza, G., Torres, J. P. & Torner, L. Twisted photons. *Nat. Phys.* **3**, 305–310 (2007).
54. C. Dada, A., Leach, J., Buller, G. S., Padgett, M. J. & Andersson, E. Experimental high-dimensional two-photon entanglement and violations of generalized Bell inequalities. *Nat. Phys.* **7**, 677–680 (2011).
55. Fickler, R. *et al.* Quantum entanglement of high angular momenta. *Science* **338**, 640–643 (2012).
56. Nicolas, A. *et al.* A quantum memory for orbital angular momentum photonic qubits. *Nat. Photonics* **8**, 234–238 (2014).
57. Ding, D.-S. *et al.* Quantum storage of orbital angular momentum entanglement in an atomic ensemble. *Phys. Rev. Lett.* **114**, 050502 (2015).
58. Zhou, Z.-Q. *et al.* Quantum storage of three-dimensional orbital-angular-momentum entanglement in a crystal. *Phys. Rev. Lett.* **115**, 070502 (2015).
59. Agarwal, G. S. Quantum statistical theories of spontaneous emission and their relation to other approaches. *Springer tracts in modern physics*: *Quantum optics* **70** (Springer-Verlag, Berlin, 1974).
60. Allen, L., Beijersbergen, M. W., Spreeuw, R. J. C. & Woerdman, J. P. Orbital angular momentum of light and the transformation of Laguerre-Gaussian laser modes. *Phys. Rev. A* **45**, 8185–8189 (1992).
61. Barnett, S. M. & Allen, L. Orbital angular momentum and nonparaxial light beams. *Opt. Comm.* **110**, 670–678 (1994).
62. Cerjan, A. & Cerjan, C. Orbital angular momentum of Laguerre–Gaussian beams beyond the paraxial approximation. *J. Opt. Soc. Am. A* **28**, 2253–2260 (2011).
63. Scully, M. O., Fry, E. S., Raymond, Ooi, C. H. & Wódkiewicz, K. Directed spontaneous emission from an extended ensemble of N atoms: Timing is everything. *Phys. Rev. Lett.* **96**, 010501 (2006).
64. Du, L. *et al.* Manipulating orbital angular momentum of light with tailored in-plane polarization states. *Sci. Rep.* **7**, 41001 (2017).
65. Oppel, S., Wiegner, R., Agarwal, G. S. & von Zanthier, J. Directional superradiant emission from statistically independent incoherent nonclassical and classical sources. *Phys. Rev. Lett.* **113**, 263606 (2014).
66. Wiegner, R., Oppel, S., Bhatti, D., von Zanthier, J. & Agarwal, G. S. Simulating superradiance from higher-order-intensity-correlation measurements: Single atoms. *Phys. Rev. A* **92**, 033832 (2015).
67. Bhatti, D., von Zanthier, J. & Agarwal, G. S. Superbunching and nonclassicality as new hallmarks of superradiance. *Sci. Rep.* **5**, 17335 (2015).
68. Bhatti, D., Oppel, S., Wiegner, R., Agarwal, G. S. & von Zanthier, J. Simulating Dicke-like superradiance with classical light sources. *Phys. Rev. A* **94**, 013810 (2016).
69. Fickler, R., Campbell, G., Buchler, B., Lam, P. K. & Zeilinger, A. Quantum entanglement of angular momentum states with quantum numbers up to 10,010. *Proc. Natl. Acad. Sci. USA* **113**, 13642–13647 (2016).
70. Hanson, R. & Awschalom, D. D. Coherent manipulation of single spins in semiconductors. *Nature* **453**, 1043–1049 (2008).
71. Buluta, I., Ashhab, S. & Nori, F. Natural and artificial atoms for quantum computation. *Rep. Prog. Phys.* **74**, 104401 (2011).
72. Sarkisyan, D. *et al.* Spectroscopy in an extremely thin vapor cell: Comparing the cell-length dependence in fluorescence and in absorption techniques. *Phys. Rev. A* **69**, 065802 (2004).
73. Carvalho, J. CdeA., Laliotis, A., Chevrollier, M., Oriá, M. & Bloch, D. Backward-emitted sub-Doppler fluorescence from an optically thick atomic vapor. *Phys. Rev. A* **96**, 043405 (2017).
74. Babazadeh, A. *et al.* High-dimensional single-photon quantum gates: Concepts and experiments. *Phys. Rev. Lett.* **119**, 180510 (2017).
75. Barreiro, J., Peters, N., Langford, N. & Kwiat, P. Quantum Electronics and Laser Science Conference, QELS 2006 Optical Society of America.
76. Olmos, B. & Lesanovsky, I. Collective photon emission from symmetric states created with Rydberg atoms on a ring lattice. *Phys. Rev. A* **82**, 063404 (2010).
77. James, D. F. V. Frequency shifts in spontaneous emission from two interacting atoms. *Phys. Rev. A* **47**, 1336–1346 (1993).

Acknowledgements

Author Contributions

M.-S. Chang and Y.-C. Chen conceived the idea, H.H. Jen conducted the derivations and numerical simulations, and H.H. Jen, M.-S. Chang, and Y.-C. Chen analyzed the results. All authors reviewed the manuscript.

Additional Information

Competing Interests: The authors declare no competing interests.

Publisher's note: Springer Nature remains neutral with regard to jurisdictional claims in published maps and institutional affiliations.